

Integrated on-chip quantum light sources on a van der Waals platform

Pietro Metuh,¹ Paweł Wyborski,¹ Athanasios Paralikis,¹ Frederik Schröder,^{1,2} Nicolas Stenger,^{1,2} Niels Gregersen,¹ and Battulga Munkhbat^{1,*}

¹Department of Electrical and Photonics Engineering, Technical University of Denmark, 2800 Kgs. Lyngby, Denmark

²NanoPhoton – Center for Nanophotonics, Technical University of Denmark, 2800 Kgs. Lyngby, Denmark

Scalable photonic quantum information technologies require a platform combining quantum light sources, waveguides, and detectors on a single chip. Here, we introduce a van der Waals platform comprising strain-engineered bilayer WSe₂ quantum emitters, integrated on multimode WS₂ waveguides with optimized grating couplers, enabling efficient on-chip quantum light sources. The emitters exhibit bright, highly polarized emission that couples efficiently into WS₂ waveguides. Under resonant p-shell excitation, we observe high-purity, waveguide-coupled single-photon emission, measured using both an off-chip Hanbury Brown-Twiss configuration ($g^{(2)}(0) = 0.003^{+0.030}_{-0.003}$) and an on-chip configuration ($g^{(2)}(0) = 0.076 \pm 0.023$). For a single output, the out-coupled single-photon count rate at the first lens reaches approximately 320 kHz under continuous-wave p-shell excitation, corresponding to an estimated waveguide-coupled rate of 1.7 MHz. These results demonstrate an efficient, integrated single-photon source and establish a pathway toward scalable photonic quantum information processing centered around nanoengineered van der Waals materials.

A vision for scalable photonic quantum information processing is the realization of a fully integrated quantum photonic circuit by integrating all the main building blocks on a single chip.^{1–3} Currently, however, state-of-the-art implementations rely on disparate material systems:⁴ silicon^{5,6} or silicon nitride⁷ for photonic circuits, III–V semiconductors for deterministic quantum emitters,^{8,9} and amorphous superconductors such as NbTiN or MoSi for single-photon detection.¹⁰ Integrating these components is possible in some circumstances,^{11,12} but it requires complex hybrid fabrication with stringent thermal and chemical compatibility, which has become a major bottleneck for scaling up photonic quantum technologies.⁴ It is therefore desirable to identify a single material platform that enables monolithic integration of all essential quantum photonic components.¹³

Transition metal dichalcogenides (TMDs) have emerged as a powerful material platform for nano- and quantum photonics owing to their strong exciton resonances, large optical oscillator strengths, and versatility afforded by van der Waals (vdW) assembly.^{14–16} Their layered structure allows deterministic exfoliation and stacking,¹⁷ enabling combination of distinct TMD materials to engineer new optical and electronic functionalities and straightforward integration with existing photonic platforms. Several mono- and bilayer TMD semiconductors, such as WSe₂^{18–21} and MoTe₂,^{22,23} can host localized quantum emitters created by strain or defect engineering, producing single photons across the visible and telecom ranges.²⁴ In parallel, the strong nonlinear coefficients of few-layer TMDs have been used for enhancing nonlinearities in established material platforms.²⁵ Multilayer TMDs also possess exceptional optical properties, including high refractive indices and low absorption over a broad spectral window

above 700 nm that support low-loss, tightly confined optical modes suitable for waveguides and photonic cavities.^{26–29} Moreover, their atomically smooth surfaces facilitate high-quality nanostructuring.³⁰ Beyond light sources and passive photonics, superconducting TMDs such as NbSe₂ have recently been explored as ultrathin single-photon detectors.^{31–33} Together, these complementary unique features position TMDs as a uniquely versatile platform in which quantum emitters, photonic circuitry, and detectors could ultimately be realized within a single vdW materials platform.

Despite substantial progress in developing individual TMD-based photonic components,^{27,34–36} a fully integrated quantum light source based entirely on a vdW platform has not yet been realized. Previous attempts to couple TMD quantum emitters to photonic circuitry have suffered from weak or uncontrolled coupling.²⁴ Monolithic integration^{37,38} is hindered due to the lack of strain needed for creating quantum emitters, while hybrid approaches^{39,40} are limited by the atomic thickness of mono- and bilayer TMDs, which is insufficient to reshape the propagating modes in the waveguide. As a consequence, demonstrations to date have relied on hybrid platforms or non-deterministic coupling strategies, and no system has yet combined a vdW quantum emitter with a vdW waveguide to realize an on-chip, waveguide-coupled single-photon source or an on-chip Hanbury Brown-Twiss (HBT) measurement.

In this work, we develop integrated quantum light sources based entirely on a nanoengineered vdW material platform. Bilayer WSe₂ quantum emitters are integrated on top of multimode WS₂ waveguides, enabling efficient waveguide coupling in a 2D–2D emitter–waveguide system. We first verify the quantum nature of a bilayer WSe₂ emitter in free space using p-shell excitation and confocal detection, obtaining $g^{(2)}(0) = 0.043 \pm 0.027$. We then examine the emission coupled through the WS₂ waveguide and collect the signal via integrated grat-

* bamunk@dtu.dk

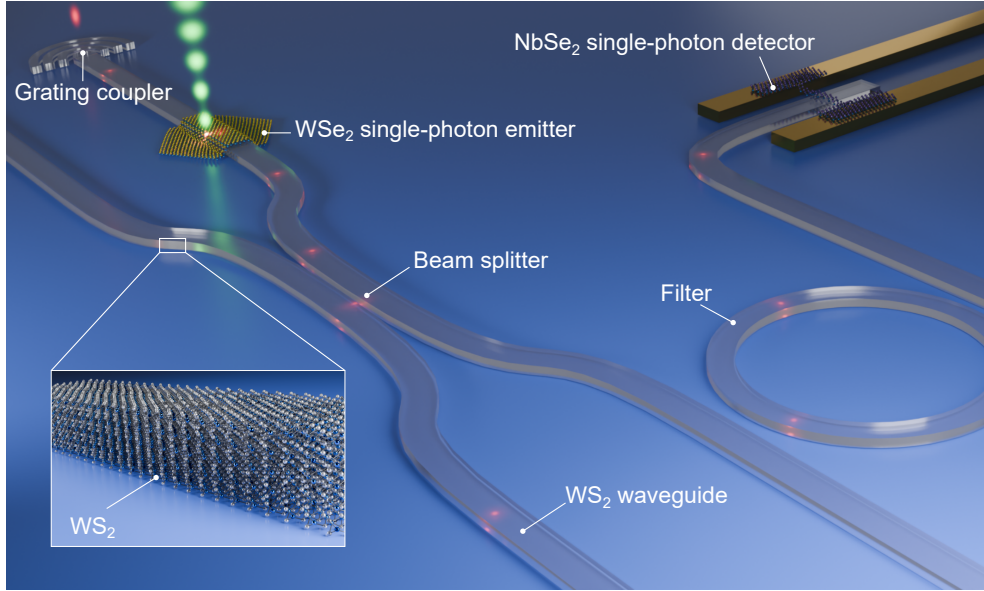


FIG. 1. TMD-based photonic integrated circuit for scalable quantum information processing. Distinct optical, electronic, and mechanical properties across different transition-metal dichalcogenides (TMDs) allow each material to serve a specialized function in an integrated quantum photonic architecture: mono- or bilayer WSe₂ as single-photon emitters, nanostructured multilayer WS₂ as high-index and low-loss photonic integrated circuits incorporating couplers, filters, beam splitters, and interferometers, and superconducting NbSe₂ nanowires as fast and efficient single-photon detectors.

ing couplers. A HBT measurement performed on the out-coupled waveguide emission retains high purity with $g^{(2)}(0) = 0.003^{+0.030}_{-0.003}$. Taking further advantage of the dual-ended geometry of our waveguides, we use the waveguide itself as a beam splitter for on-chip HBT measurements. When the emitter is coupled efficiently to the waveguide, its emission splits and propagates toward both grating couplers, so that single photons can be collected simultaneously from each output port. High single-photon purity is preserved with this configuration ($g^{(2)}(0) = 0.076 \pm 0.023$). Moreover, we estimate an out-coupled single-photon rate at the first lens of approximately 320 kHz (240 kHz) from the first (second) grating coupler under p-shell excitation. Under the assumption of a grating extraction efficiency of 18.8%, the upper limit obtained via finite-difference time-domain (FDTD) simulations, this translates to a waveguide-coupled rate of approximately 1.7 MHz (1.28 MHz). These results constitute the first demonstration of an integrated single-photon source where both the active quantum emitter and the passive photonic circuitry are realized entirely from vdW materials. This achievement promotes a vdW-centered platform for quantum photonics and paves the way toward monolithic, 2D material-based integrated quantum photonics.

I. Our vision: a versatile van der Waals platform for quantum photonics

Figure 1 illustrates our vision of a photonic integrated circuit made primarily of TMD materials with complementary optical and electrical functionalities.^{41,42} Within this platform, strain-engineered TMDs serve as on-demand quantum light sources. Localized quantum emitters in WSe₂ have been widely reported,^{19,43} and are believed to originate from hybridized energy lev-

els of defects in strained material.⁴⁴ High-purity single-photon emission has been observed in both monolayer and bilayer WSe₂, with bilayers offering reduced background photoluminescence while maintaining high emitter brightness.^{45–47} In this concept (Figure 1), local strain is applied by transferring WSe₂ onto nanostructured slab waveguides, where edge-induced wrinkles naturally form, inducing quantum emitters.³⁴

Photonic circuits are realized with nanostructured multilayer TMDs, such as WS₂, which can be patterned with established nanofabrication techniques^{30,48} and offer high refractive index and low optical loss from 750 nm up to the telecom range, making them well suited for integrated photonics.²⁷ Other essential photonic components, such as grating couplers, beam splitters, cavities, and spectral filters can all be implemented within a unified vdW material platform.^{30,49} Beyond sources and passive circuitry, superconducting vdW materials such as NbSe₂ can be patterned into integrated superconducting-nanowire single-photon detectors (SNSPDs),^{31,32} whose high detection rates, high efficiency, and low timing jitter excel among single-photon detector classes.

Such a platform can be developed without the need for complex physical or chemical vapor deposition techniques, which are often a limiting factor in the monolithic or hybrid fabrication of all the circuit components in a single photonic chip. The lack of dangling bonds in their lattice results in an effective hybrid integration approach,¹³ where vdW films can be precisely transferred on any photonic circuit with pre-patterned features and devices for generating,^{35,39,50} guiding,^{27,49} and detecting^{31,32} single-photon states, thus making vdW materials compatible with other existing circuit platforms.

II. Van der Waals photonic devices: waveguides and grating couplers

We begin by establishing the passive optical waveguides and grating couplers based on nanostructured multilayer WS₂ as building blocks for integrated photonics. The proposed waveguide geometry consists of multimode WS₂ slab waveguides that are 500 nm wide and 150 nm tall, to enhance the mode overlap with any dipole-like quantum emitter located outside the slab waveguide. Figures 2a,b show the dispersion relation of the propagating modes and their electric field profile at 802 nm, respectively. Despite separating the modes into transverse-electric (TE) and transverse-magnetic (TM) for their features at shorter wavelengths, it is worth noting that, at 802 nm, most higher-order modes are hybrid, and therefore have a variable TE/TM polarization ratio. The fabrication process for the presented waveguides begins by mechanical exfoliation of WS₂ flakes, which are initially filtered by their thickness with optical reflectometry; when suitable homogeneous flakes at the desired thickness are found, they are transferred onto Si chips with a 2 μm layer of SiO₂ and pre-patterned alignment markers. The photonic circuits are then fabricated by transferring an electron-beam resist pattern onto the flake via reactive-ion etching (RIE), before removing the resist mask. Details of the fabrication are given in the Methods section and Supplementary Figure 1. The resulting waveguides are characterized by a smooth and homogeneous surface (given by the pristine WS₂ flake) and limited sidewall roughness or etching residues, as reported in atomic force microscopy (AFM) and scanning electron microscopy (SEM) images in Figure 2c,d.

Initially, a set of three short waveguides (21 μm) with a single grating coupler, whose design is described later in this section, was patterned to illustrate the coupling mechanisms (Figure 2d). As shown in Figure 2e, a single-mode fiber-coupled broadband light beam can be launched into the waveguide by scattering on a bare edge (i); the emission can then couple out of the grating coupler and be collected by the same objective, revealing a smaller bright spot at the opposite end of the waveguide. If the beam spot is moved slightly to the right, no light can scatter through the waveguide (ii). Light can also be injected via the grating coupler (iii), and emission can be observed because of the up-scattered light from the opposite end. Therefore, scattering from the waveguide ends enables coupling to and from a high-numerical aperture (NA) objective even without additional structures (iv), despite the reduced efficiency.

To characterize the propagation properties of a 20 μm -long waveguide (shown in Figure 2c), we perform scattering-type scanning near-field optical microscopy (sSNOM) measurements between 1120–1190 nm in increments of 10 nm (see Methods). For each wavelength, we extract the momentum of the propagating waves in the system.^{51,52} Plotting these momentum values as a function of the excitation wavelength enables

us to reconstruct the dispersion relation of the waveguide modes, shown in Figure 2f. This analysis reveals a mode with wavenumber $q = 2.45 \mu\text{m}^{-1}$ at wavelength of $\lambda = 1190 \text{ nm}$, corresponding to an effective refractive index of $n_{\text{exp}} = 2.90$.

As a comparison, the refractive index of the fundamental TE mode in a WS₂ slab waveguide with $500 \times 175 \text{ nm}$ in cross-section and 40 nm of overetch on SiO₂ is $n_{\text{num}} = 2.99$, which is in good agreement with the observed results with sSNOM measurements. The other major feature in the near-field spectral map matches a refractive index of $n_{\text{sub}} = 1.44$, which corresponds to a substrate mode propagating in the silicon oxide layer.

To characterize waveguide-coupled quantum emitters in far-field measurements, it is convenient to use a single optical path for excitation and collection, which is focused or collimated with a low-temperature, high-NA objective, thereby reducing the complexity of the experimental setup and removing the need for independent optical fibers for each input and output. Figure 2e, for instance, shows how the light source can be launched through one grating coupler and exit the other, where the collection spot can be aligned to. However, injecting light into the waveguide from an objective-focused beam is inherently less efficient than optical fiber coupling, because phase matching at the grating coupler can only be achieved at specific angles.⁵³ In addition, typical grating coupler designs are optimized for the size of a fiber mode and feature a tapered waveguide to adiabatically alter the field confinement.⁵³ Therefore, we focus on a grating coupler design optimized for microscope operation. The starting point was a compact silicon nitride design for microscopy systems consisting of concentrical half rings.⁵⁴ Despite the shorter operational wavelength in the referenced work (632.8 nm), the effective refractive index of silicon nitride is considerably smaller than our proposed WS₂ waveguide, which is the main factor of deviation in our proposed design. Moreover, given our use of a SiO₂ substrate, no supporting bridge for suspended features was required. The single-step etching process was maintained, thus fixing the etch depth of the grating coupler to the waveguide height.

Numerical modelling of the grating coupler was carried out with FDTD simulations (see Methods). Since the quantum emitters are directly excited with an out-of-plane laser beam, the in-coupling efficiency from the objective to the waveguide is of secondary importance. Therefore, the main figure of merit for the optimization was the out-coupling efficiency with a fixed numerical aperture (NA = 0.81) of a propagating mode inside the waveguide. This figure of merit is the product of two quantities: the upward-scattered transmittance from the grating, and the fraction of the far field within the objective aperture. The latter benefits from a narrow out-coupled beam, but can be increased by using a larger numerical aperture. Figure 2g shows an example of the far-field electric field distribution for TE₀₀ at 800 nm; in this case, most of the upward-scattered radiation lies

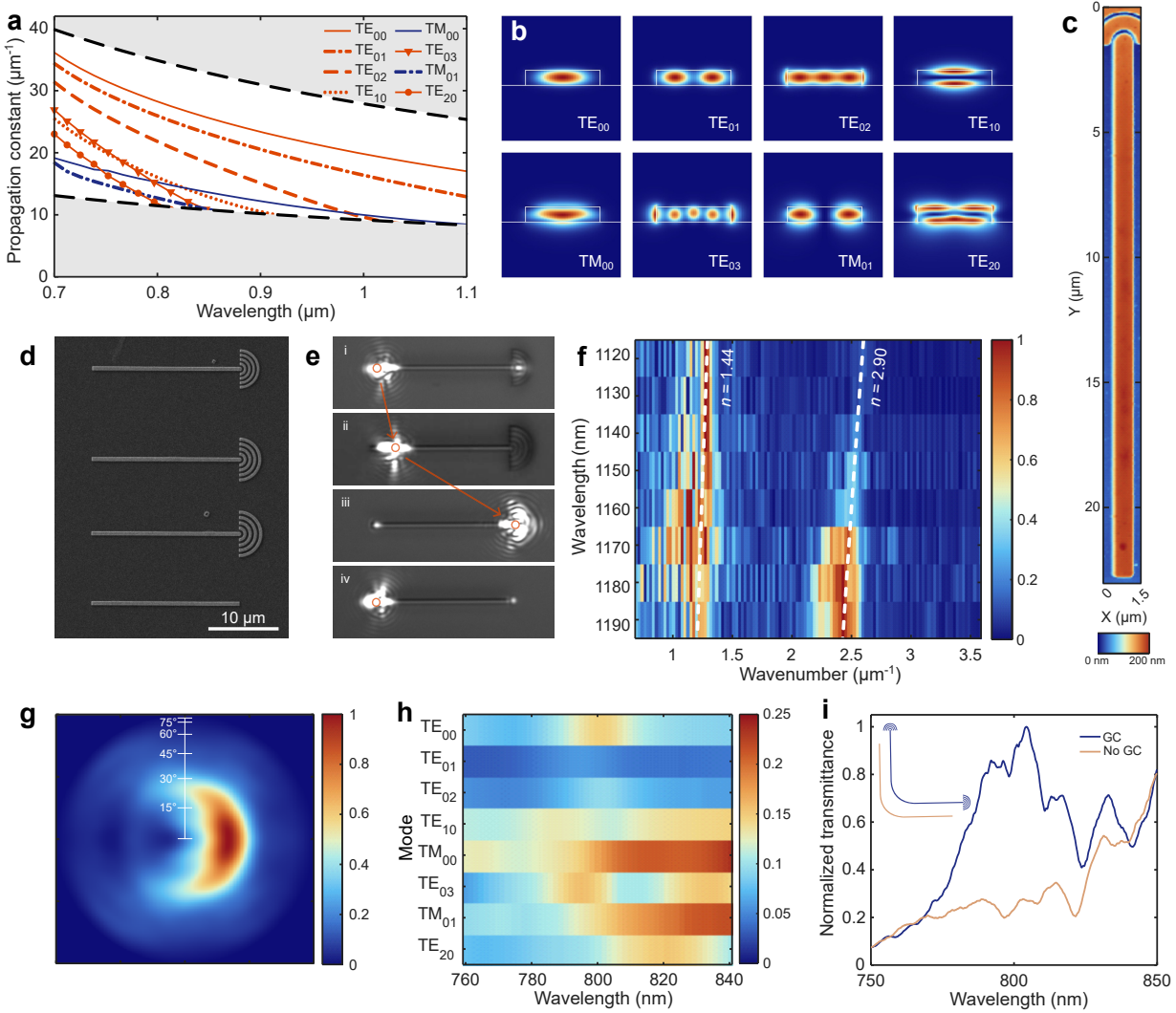


FIG. 2. Nanostructured WS₂ for on-chip waveguides. (a) Dispersion relation of a $500 \times 150 \text{ nm}$ WS₂ slab waveguide on a SiO₂ substrate, showing all propagating modes with a cut-off wavelength above $\lambda = 800 \text{ nm}$. The dashed black lines mark the propagation constant in bulk WS₂ and SiO₂. (b) Electric field intensity profile at $\lambda = 802 \text{ nm}$ for each propagating mode shown in (a); the waveguide and substrate cross-sections are outlined in white. (c) Atomic force microscopy trace of the $500 \times 175 \text{ nm}$ waveguide used for scanning near field optical microscopy, showing a slab waveguide with minimal surface roughness. (d) Scanning electron microscopy image of short $500 \times 150 \text{ nm}$ slab waveguides with variable grating coupler pitch or no grating coupler (bottom waveguide). (e) Optical microscopy image of two of the waveguides shown in (d) under illumination with a broadband source; the empty orange circle indicates the beam spot. Light can be coupled in the waveguide by edge scattering (i, iv) or grating coupling (iii) and observed on the opposite end; no light is coupled by irradiating the surface of the waveguide (ii). (f) Dispersion relation of the TE modes measured with near-field microscopy (sSNOM) over the waveguide in (c) at decreasing photon wavelengths, from 1190 to 1120 nm . The two dashed lines matching the spectral features correspond to an effective refractive index of 2.90 (propagating mode) and 1.44 (SiO₂ substrate mode). (g) Far-field distribution of the upward-coupled fundamental TE mode at $\lambda = 800 \text{ nm}$ from the proposed grating coupler design, obtained via FDTD modelling; the fundamental TM mode shares a similar pattern. All the light within a half-angle of 54.1° can be collected with an objective with NA = 0.81. (h) FDTD modelling of the collection efficiency spectra for the propagating modes with the proposed grating coupler design. (i) Comparison of the total transmittance between grating coupling (blue) and side-scattering coupling (yellow) through a $\approx 60 \mu\text{m}$ -long WS₂ waveguide. The spectra are ten point-averaged and normalized by the grating-coupled transmittance value at 800 nm . The inset shows an illustration of the waveguides characterized in the measurement.

within the cone with a half-angle of 53.1° , corresponding to the objective NA. The TM₀₀ mode features a similar pattern, reported in Supplementary Figure 2. The op-

timized grating coupler after the parameter sweeps has four half-rings, a pitch of 780 nm , and a duty cycle of 55%. The total out-coupling efficiency spectrum after

the parameter sweeps is shown in Figure 2h for all the propagating modes at 800 nm. The extraction efficiency averaged over the propagating modes is 12.5% at 802 nm, the peak being 18.8% for the TM_0 mode, and it is mainly limited by two main factors: the very high index contrast between WS_2 and air, which could be improved by letting the etch depth vary (thus requiring a two-step etching process),^{53,55} and the asymmetry between the air cladding and the substrate. A suspended design or a reflective substrate would therefore improve the coupling efficiency further.⁵⁴

Light injection through the waveguide was characterized by comparing the spectral transmittance of a bent 60 μm -long waveguide with and without grating couplers (Figure 2i) when launching a single mode-coupled broadband beam through one end and measuring the spectrum on the other. Additional spectra with an extended range are given in Supplementary Figure 2. Remarkably, we observe a maximum around 800 nm within the range 750–850 nm, and the structure with the grating coupler has a consistently higher transmittance throughout the displayed spectral range.

III. Integration with quantum emitters

Having examined the fabricated circuits, we integrated the 60 μm -long waveguide characterized in Figure 2i with quantum emitters by first transferring a thin layer of hexagonal boron nitride (hBN) on a waveguide to partially cover it, followed by a second transfer of bilayer WSe_2 . By having a thin layer of hBN between WS_2 and WSe_2 , the likelihood of the bilayer breaking during transferring is decreased, while maintaining proximity between the two materials to facilitate the emitter coupling into the waveguide. Once the stack was transferred, the sample was cooled down to $T \approx 4$ K. Initially, we found quantum emitters by scanning a focused laser along the waveguide and monitoring the confocal photoluminescence; once a narrow spectral line is observed, the collection spot can be repositioned to either grating coupler to confirm the coupling of the emitter through the waveguide, as illustrated in Figure 3a. Even without measuring the spectra, photoluminescence can be imaged with a camera after filtering out the excitation source, as shown in Figure 3b, where the laser is positioned on top of the quantum emitter characterized in Figure 3d–g. Additional photoluminescence images are provided in Supplementary Figure 3.

The coupling of an emitter—here modelled as a dipole source—into the waveguide is highly dependent on the position and orientation of the emitter. To analyze the coupling efficiency, we use FDTD simulations (Methods) to calculate the coupling between a dipole source (positioned 5 nm above the waveguide to simulate the hBN thickness) and each of the propagating modes (Supplementary Figure 4). The results show that the leakier modes (either higher-order TE modes or any TM mode)

have an overall stronger coupling to the dipole emission due to the larger overlap with the field profile (shown in Figure 2b). The efficiency is also highly dependent on the dipole orientation: Figure 3c reports the total coupling efficiency to a guided mode at each dipole orientation axis. Due to the hybrid polarization of some propagating modes, coupling is possible not only for an in-plane dipole orthogonal to the waveguide axis (y direction in the plot), but also for a dipole oriented along the waveguide (x) and for an out-of-plane dipole (z), albeit with a reduced efficiency. While the dipole orientation in strained WSe_2 flakes is known to follow the wrinkle orientation,²¹ transferring a flake onto a slab waveguide with a bottom hBN layer did not seem to induce a preferred strain direction. Therefore, all dipole orientations have been considered in the analysis. The simulation has also been carried out with a dipole along the side of the waveguide rather than above it (Supplementary Figure 5).

We now focus on a spectral line at $\lambda = 802$ nm, positioned where the excitation laser is aligned to in Figure 3b, and compare two excitation schemes: above-band excitation (ABE) and p-shell excitation (PSE). Once an emitter has been found, the pump wavelength is detuned 10–30 nm below the emission line, which is separated enough to enable efficient spectral filtering of the excitation source. Once a higher-energy discrete level of the emitter is reached (here, at $\lambda_p = 783$ nm), a considerable increase in the emitter brightness is observed, both with a confocal collection spot and at the grating couplers (Figure 3d). Two spectra of the same emitter collected at the grating couplers are compared in Figure 3e with a 650 nm continuous-wave (CW) laser and a 783 nm CW laser at near-saturation pump power. Brighter emission is achieved under PSE, while simultaneously reducing the spectral background from higher-energy states.⁵⁶ This results in stronger photoluminescence than previous examples of waveguide-coupled TMD single-photon emitters,^{34,50} which can be partly attributed to a larger field overlap between the emitter and the guided modes.²⁴ Incidentally, bilayer WSe_2 transferred on WS_2 waveguides without a bottom hBN flake coupled weakly to the waveguide (Supplementary Figure 6), similarly to previous reports,³⁴ hinting at hBN affecting the charge environment and strain profile in WSe_2 .⁵⁷ The integrated counts under the spectral line show roughly an order of magnitude of difference at equal pump power, while the emitter linewidth is comparable, if slightly narrower, under PSE (Figure 3f). Furthermore, the decay time of this emitter is reduced from $\tau_{\text{ABE}} = (55.0 \pm 1.1)$ ns to $\tau_{\text{PSE}} = (31.1 \pm 0.4)$ ns (Supplementary Figure 7).

Having established the efficacy of PSE, we evaluate additional spectral properties of waveguide-coupled WSe_2 emitters. Time-series photoluminescence spectra (Supplementary Figure 7) show little spectral wandering, which could be further reduced by stabilizing the charge environment.⁵⁷ In addition, polarization-resolved measurements confirm the polarized nature of the emitter,

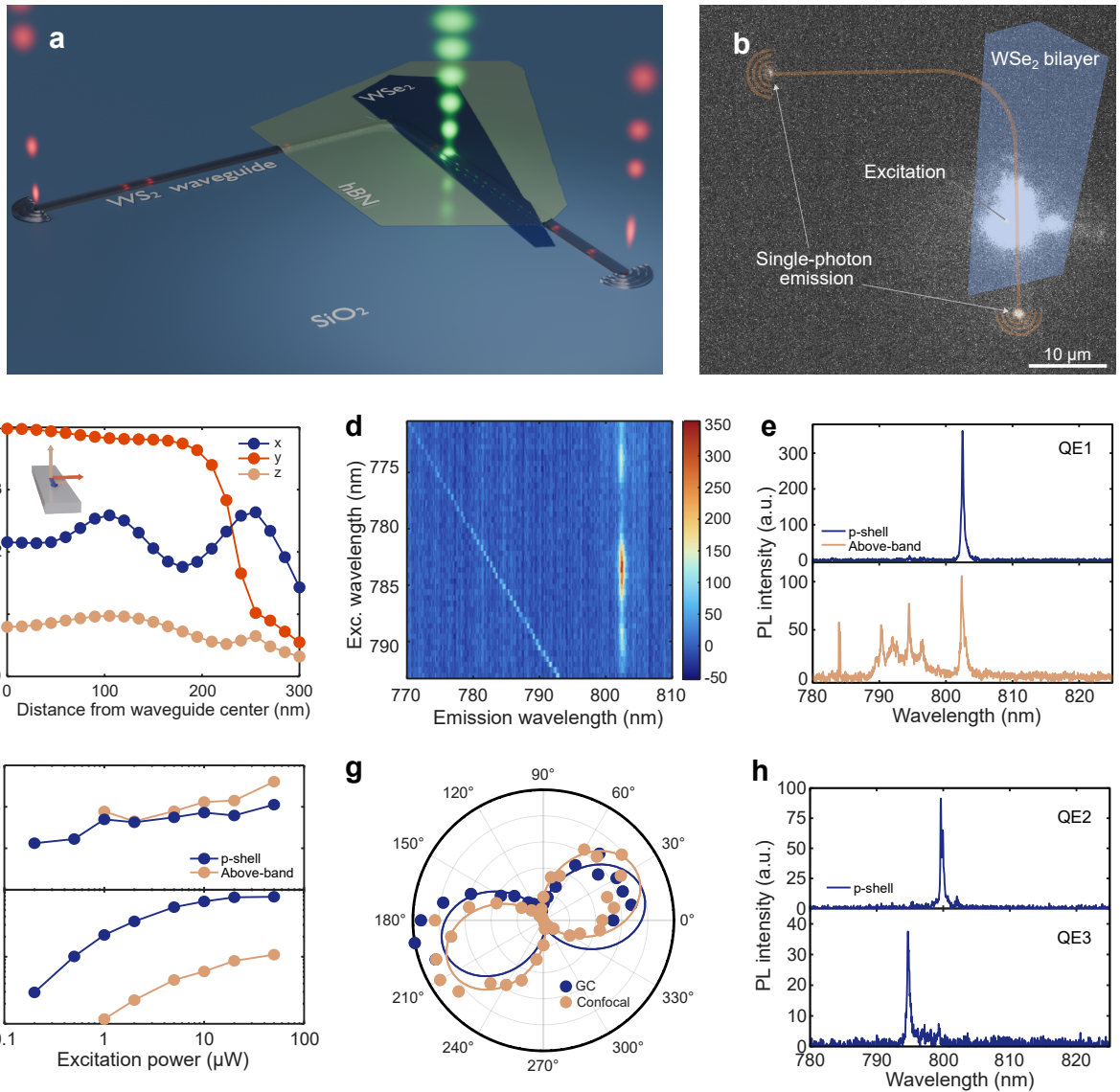


FIG. 3. Integration of WS_2 waveguides with hBN/WSe₂ heterostructures for on-chip coupling of single photons. (a) Artistic illustration of the characterized device, consisting of a $60\ \mu\text{m}$ -long WS_2 waveguide with a 90° bend and grating couplers, with a thin ($< 5\ \text{nm}$) hBN layer and a WSe₂ bilayer transferred on top. By optically exciting a quantum emitter in the WSe₂ bilayer, single-photon states couple to a propagating waveguide mode and are then collected via the grating couplers. (b) Photoluminescence emitted by the transferred bilayer flake with the excitation laser centered on a quantum emitter; the waveguide and a portion of the bilayer are overlapped in the image for reference. Photoluminescence is observed on both the excitation spot and the two grating couplers. (c) Simulated coupling efficiency between an electric dipole $5\ \text{nm}$ above the waveguide and a propagating mode as a function of the distance from the vertical symmetry axis of the waveguide cross-section; the coupling is calculated with the dipole oriented along each main axis. (d) Photoluminescence spectral map of a quantum emitter at $\lambda = 802\ \text{nm}$, collected at the upper grating coupler; the emitter can be excited via p-shell excitation, showing peak emitter brightness with excitation laser at $\lambda_p = 783\ \text{nm}$. The partially-filtered laser line is intentionally shown. (e) Emission spectra at the upper grating coupler obtained via p-shell and above-band excitation of the quantum emitter; p-shell excitation suppresses the majority of the background emission and increases the emitter brightness. (f) Excitation power-dependent emission intensity (integrated counts per second at the spectrometer, logarithmic scale) and spectral linewidth of the quantum emitter at the upper grating coupler under the two excitation schemes. (g) Polarization-dependent emission intensity at the upper grating coupler or confocal to the excitation laser under p-shell excitation, fitted with a sinusoidal curve. (h) Additional examples of spectral lines coupled through the waveguide and collected at a grating coupler.

which is preserved even for waveguide-coupled emission. The degree of linear polarization (DOLP) at the upper grating coupler and confocal to the emitter, calculated

as $(I_{\text{max}} - I_{\text{min}})/(I_{\text{max}} + I_{\text{min}})$, gives $(84 \pm 18)\%$ and $(98^{+2}_{-8})\%$, respectively, producing comparable results to

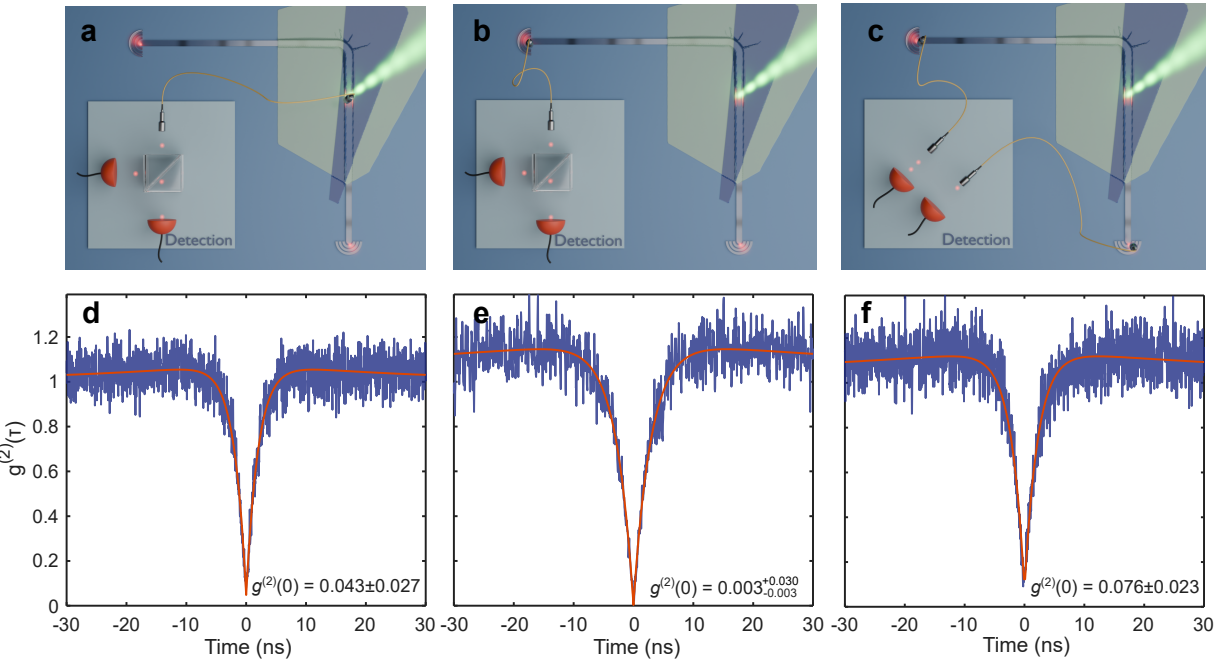


FIG. 4. On-chip waveguide-coupled single-photon purity. (a-c) Simplified illustration of the Hanbury Brown and Twiss (HBT) experimental setup realized with (a) the collection spot confocal to the excitation source and an external beam splitter before the detectors; (b) the collection spot at one grating coupler with an external beam splitter before the detectors; (c) a collection spot at each grating coupler, so that the HBT effect can be observed without an external beam splitter. (d-f) Continuous-wave second-order autocorrelation traces obtained with the respective setup; the traces are plot with a three-point moving average, and show signatures of photoluminescence blinking. All configuration exhibit high single-photon purity at zero time delay.

other strain-engineered WSe₂ emitters.²¹ From the polarization axis, the dipole axis can be inferred to have a parallel component to the waveguide. However, an out-of-plane dipole component cannot be excluded, as emission would be mostly inaccessible by the objective, yet could still couple to a waveguide mode. Both these dipole orientations couple best with TM or hybrid modes, highlighting their importance for this work. Additional polarization-dependent measurements are discussed in Supplementary Figure 8.

To further assess the potential of generating quantum emitters with this process, additional spectra from other waveguide-coupled emitters were characterized by scanning the laser along the waveguide (Figure 3h). Bright spectral lines between 795 and 800 nm were observed when tuning the excitation wavelength and collecting the emission from a grating coupler, supporting WS₂ waveguides as a robust platform for on-chip coupling of vdW emitters.

IV. On-chip second-order correlation measurement

To verify the single-photon nature of the observed emitter, we evaluated the second-order autocorrelation function $g^2(\tau)$ under different HBT setup configurations. Single photons are first collected confocally to the exci-

tation source, as shown in the illustration of Figure 4a. The signal is then split into two arms with a beam splitter and independently detected with a superconducting-nanowire single-photon detector (SNSPD), whose events are correlated with a time-to-digital converter, producing the autocorrelation trace shown in Figure 4d. Since a combination of photon bunching and antibunching is observed, the dataset is fitted with a three-level model.⁵⁸ The bunching effect, which is more visible in the extended data presented in Supplementary Figure 9, originates from luminescence blinking and is likely a consequence of charge fluctuations.⁵⁷ The fitted curve gives a zero-delay second-order correlation of $g^{(2)}(0) = 0.043 \pm 0.027$, demonstrating that the characterized emitter is a source of single photons with high purity.

The measurement is repeated by moving the collection spot to one of the grating couplers (Figure 4b), thereby correlating the waveguide-coupled emission. With this dataset, the purity of the single-photon state ($g^{(2)}(0) = 0.003^{+0.030}_{-0.003}$) is further increased and nearly reaches the unity limit. We attribute the increased purity compared to the configurations of Figure 4a to a slightly lower excitation power and better waveguide coupling of the emitter compared to background emission.

In the final configuration, the beam splitter in the HBT setup is removed, and a second collection spot is implemented and aligned with the other grating coupler (Fig-

ure 4c). Single-photon emission couples to a propagating mode in both waveguide directions, so that the waveguide itself can be used as an on-chip beam splitter. In addition to simplifying the macroscopic experimental setup, this improves the robustness of the second-order autocorrelation measurement, which is obtained by correlating photons at two separate waveguide ports, rather than halving the photon stream of a single one. The resulting measurement confirms the preserved purity of the quantum emitter ($g^{(2)}(0) = 0.076 \pm 0.023$) and provides, to our knowledge, the first example of on-chip HBT measurement with vdW single-photon sources.

We conclude this section by commenting on the emitter brightness. The single-photon count rate at saturation measured by the SNSPD during the autocorrelation measurements yielded approximately 20 and 15 kHz for the upper and lower grating coupler, respectively. Accounting for the losses in the transmission setup (Supplementary Note 10), we estimated the single-photon rate at the first lens to be 320 and 240 kHz for the respective grating coupler. Since the maximum extraction efficiency from the grating coupler is 18.8%, as calculated with FDTD modelling in Figure 2h, we estimate a waveguide-coupled single-photon rate of 1.7 MHz and 1.28 MHz along the two directions. We note that this is a conservative estimation, as fabrication imperfections and multimode coupling render the simulated extraction efficiency value an upper bound. As a comparison, the confocal count rate at the first lens is evaluated at 1.6 MHz. Given an average re-excitation time of 31.1 ns (given by the measured decay time), the total waveguide-coupled quantum efficiency is estimated at 9.3%, highlighting the effective coupling mechanism in the presented vdW system and the emitter brightness. Further improvements would be achievable via electrical biasing, which could increase spectral stability and tuning. In addition, the emitter brightness and indistinguishability could be further improved by integration with a high- Q optical cavity^{37,59,60} and advanced excitation schemes.^{47,61}

V. Conclusions

In this work, we demonstrated integrated on-chip quantum light sources entirely based on a van der Waals platform. The integration of bilayer WSe₂ quantum emitters with multimode WS₂ waveguides enables efficient on-chip coupling of single photons. We demonstrate high-purity, waveguide-coupled single-photon emission and comprehensively characterize its polarization properties and decay dynamics. Multiple single-photon emitters are shown to couple efficiently to the WS₂ waveguide, highlighting the robustness and scalability of the platform. Moreover, the bidirectional coupling of the WS₂ waveguide is exploited to realize an integrated Hanbury Brown-Twiss configuration, establishing an on-chip second-order correlation experiment. The estimated MHz-level waveguide-coupled count rates indicate effi-

cient emitter-waveguide coupling and underscore the potential of the vdW platform for bright on-chip quantum light sources. Extending this platform to incorporate van der Waals single-photon detectors, phase modulators, and interferometric components would enable a promising route toward fully integrated quantum photonic circuits, paving the way for scalable quantum information processing based entirely on nanoengineered two-dimensional materials.

Methods

A. Numerical modelling

Eigenmode modelling. Modelling of the propagating modes and the dispersion relation were carried out with a finite-difference eigenmode solver in Ansys Lumerical. For the calculations, a dispersive complex refractive index was fitted for each material; for WS₂, an anisotropic index was implemented.⁴²

Grating coupler simulations. The design of the grating coupler and the calculations of waveguide-objective coupling, far-field maps, and dipole-waveguide coupling were simulated with the FDTD solver in Ansys Lumerical. The initial structure of the grating coupler was adopted by another work⁵⁴ and optimized by sweeping ring period, duty cycle (i.e., the ratio between the ring width and the ring period), and number of rings. The out-coupling efficiency was calculated by calculating the transmittance from each propagating mode to a field monitor above the grating coupler; the transmittance was then integrated within the light cone of an objective with NA = 0.81, corresponding to a half-angle of about 53.1°.

Dipole-waveguide coupling simulations. Dipole-waveguide simulations were modelled in Ansys Lumerical by calculating the projection of each propagating mode in the transmittance from a dipole source into the slab waveguide. Due to the variable dipole power emitted by the source (which is highly dependent on the dipole position relative to the waveguide), the coupling efficiency was normalized by the Purcell factor at each position, so that the coupling relative to the real emitted power can be evaluated. The total coupling efficiency is calculated by summing the contribution of all eight propagating modes for each dipole axis orientation.

B. Nanofabrication

Substrate preparation. The substrates are prepared by thermally growing 2 μm of SiO₂ on silicon and patterning alignment markers with a negative UV resist (AZ nLOF 2020) and electron-beam evaporation of 5 nm of titanium, followed by 50 nm of gold. The metal is lifted off in an ultrasonic bath of MICROPOSIT Remover 1165 and rinsed in isopropyl alcohol and water.

Exfoliation and transferring. WS_2 , hBN, and WSe_2 (HQ Graphene) are exfoliated using the same stamping technique.¹⁷ Semiconductor wafer tape (Nitto SWT 20+R) is used to initially exfoliate and thin down large flakes from a bulk crystal. Polydimethylsiloxane (PDMS) stamps on glass slides are then used to exfoliate the crystal into smaller flakes, which are selected by thickness and homogeneity. The thickness of WS_2 was measured by fitting reflectivity spectra from confocal illumination of the flake on the PDMS stamp with a broadband source. Thin flakes of hBN were selected by their optical contrast under an optical microscope, and bilayer WSe_2 was identified by room-temperature photoluminescence with a blue LED.

WS_2 flakes are positioned and transferred onto the substrate with a transfer station (HQ Graphene Systems HQ2D MAN), where the substrate is heated to 70°C to overcome the adhesion of the flake to PDMS upon contact. Three baths of acetone, isopropyl alcohol, and deionized water are used to clean the sample from contaminants at the end of the transfer process. After transferring the flakes, the fit was confirmed with a stylus profilometer (Bruker Dektak XTA). The same method has been used to transfer hBN and WSe_2 after patterning the waveguides and removing the resist mask.

Patterning of WS_2 waveguides. WS_2 flakes were patterned with electron-beam lithography by spin coating an adhesion promoter (Microchemicals TI Prime) and negative resist (Allresist AR-N 7520) and exposing it (Raith eLINE at 30 kV or JEOL JBX-9500FS at 100 kV). A thin aluminium layer (10 nm) was thermally evaporated on the samples processed at 100 kV before the exposure. Aluminium was removed with AZ 726 MIF (2.38% tetramethylammonium hydroxide) in 30 s and rinsed in water, while the resist was developed with Allresist AR 300-47 in 1 min and rinsed in water. The resist was descummed in an oxygen plasma for 30 s. The pattern was transferred to the WS_2 flake with an ICP-RIE tool (SPS M/PLEX ICP-RIE) in a CHF_3 - and Ar-based chemistry (40 sccm flow for each gas, 10 mTorr pressure, 150 W coil power and 25 W platen power).

C. Characterization

Near-field measurements. A scattering-type scanning near-field optical microscope (attocube neaSCOPE) in reflection mode was used to map a 500 × 175 nm WS_2 slab waveguide with 50 nm of SiO_2 overetch. The incident light from a tunable laser (Sacher Lasertechnik Group TEC-520-1180-030) is focused by a parabolic mirror on a platinum-iridium coated silicon AFM probe tip (NanoWorld ARROW-NCPT) operating in tapping mode. The excitation light impinges in the YZ plane (see Figure 2c) at an angle of approximately 45°. The scattered light is detected with a photodiode (Newport 2053-FC). Both the excitation and the scattered light are filtered with a co-polarized linear polarizer, aligned in s-

polarization. The signal recorded by the photodiode is demodulated at the third harmonic order of the tip tapping frequency.^{62,63} Together with a pseudo-heterodyne detection scheme,⁶⁴ this allows retrieval of the near-field amplitude while the far-field signal is largely suppressed.

Waveguide characterization. Room-temperature coupling to the waveguide was performed with a home-made confocal photoluminescence setup by using a filtered broadband source (Thorlabs OSL2IR) coupled to a single-mode fiber (Thorlabs P3-780A-FC-2), a 50× objective (Nikon LU Plan Fluor, NA = 0.8), and an infrared spectrometer (Andor Kymera 328i). The sample was imaged with a CMOS camera (Thorlabs CS165MU/M).

For low-temperature characterization measurements, the sample was loaded in an optical, closed-cycle vacuum cryostat (attocube attoDRY800) with a nano-positioner and a base temperature of $T \approx 4$ K. At low temperature, the transmission measurements were carried out with the same light source, but with a visible-light spectrometer (Horiba iHR 550) and imaging camera (Tucson Dhyana 400D). A low-temperature objective (attocube LT-APO/NIR/0.81, NA = 0.81) is used to focus the light on the sample surface. The spectra were post-processed with a ten-point moving average to smoothen the signal, and are normalized by dividing the traces with a reference spectrum of a reflective gold mirror.

Photoluminescence measurements. Bilayer WSe_2 is illuminated with either a 650-nm diode laser (PicoQuant LDH-D-C-650) in continuous-wave or pulsed mode for above-band excitation, a tunable (770-795 nm) CW laser (Toptica DL PRO) for continuous-wave p-shell excitation, and a tunable femtosecond laser (Coherent Chameleon Ultra II) for pulsed p-shell excitation. The laser polarization is controlled with a half-wave plate and a linear polarizer before entering the optical window of the cryostat and is focused by the same low-temperature objective. The same objective collimates the photoluminescence signal, which is filtered from the laser pump with different configurations of bandpass or longpass filters. Photoluminescence mapping was performed with the camera and the spectrometer mentioned above.

The polarization-resolved measurements were fitted with the following function:

$$I(\phi) = a \sin^2(\phi - \phi_0) + b. \quad (1)$$

The error in the degree of linear polarization, calculated as $a/(a + 2b)$, is given as a 95% confidence interval and is calculated by propagating the error from (1).

Decay time and second-order correlation measurements. Time-correlation measurements were carried out by detecting the signal using a superconducting nanowire single-photon detector (ID Quantique ID281). Temporal events for time-resolved photoluminescence and second-order autocorrelation measurements were correlated with a time-to-digital converter (Swabian Instruments Time Tagger Ultra).

All second-order correlations were measured with the tunable CW laser at $\lambda_p = 783$ nm. The presented raw

data are processed with a three-point average. The fitting was carried out with a three-level model, which is described by the following equation:

$$g^{(2)}(\tau) = 1 - (1 + a)e^{-|\tau|/\tau_1} + be^{-|\tau|/\tau_2}, \quad (2)$$

where τ_1 and τ_2 are antibunching- and bunching-related time constants, respectively. The error in the second-order correlation at zero delay is given as a 95% confidence interval, and is calculated as a sum of the errors of a and b .

Sample imaging. Optical microscopy images were taken in confocal microscopes with various objectives and cameras. The topography of the photonic circuits and of the transferred hBN and WSe₂ was characterized with a scanning electron microscope (Zeiss Supra 40 VP, 5 kV, SE2 detector) and an atomic force microscope (Bruker Dimension Icon, tapping mode with Tap150Al-G tips). Samples containing bilayer WSe₂ flakes were imaged only at the sample end-of-life to avoid inducing defects or charging the bilayer before characterization.

Acknowledgements

P.M., P.W., A.P., N.G., and B.M. acknowledge support from the European Research Council (ERC-StG “TuneTMD”, grant no. 101076437) and Villum Fonden (project no. VIL53033). The authors also acknowledge the European Research Council (ERC-CoG “Unity”, grant no. 865230), the TICRA foundation, the Innovation Fund Denmark (QLIGHT, no. 4356-00002A), and the cleanroom facilities at the Danish National Centre for Nano Fabrication and Characterization (DTU Nanolab). F.S. and N.S. are supported by the Danish National

Research Foundation through NanoPhoton—Center for Nanophotonics, Grant No. DNRF147. N.S. acknowledges funding by the Novo Nordisk Foundation NERD Programme (Project QuDec NNF23OC0082957). Finally, P.M. acknowledges Ryo Mizuta Graphics for the Optical Components Pack asset, which was partially used for the artistic illustrations in Figure 4.

Author contribution

P.M. performed the numerical modelling, fabricated the waveguides, and processed and analyzed all the presented data. F.S. performed the sSNOM characterization. A.P. and P.M. transferred the hBN/WSe₂ stacks on the waveguides. P.W. and P.M. performed the optical characterization of the waveguides and the quantum emitters. B.M. supervised and coordinated the project. P.M., P.W., A.P., and B.M. wrote the manuscript with input from all co-authors.

Competing Interests

The authors declare they have no competing interests.

Data availability statement

The data supporting the findings of this study are available within the main manuscript and its supporting information files. Additional data are available from the corresponding authors upon reasonable request.

References

- [1] O’Brien, J. L., Furusawa, A. & Vučković, J. Photonic quantum technologies. *Nature Photon* **3**, 687–695 (2009).
- [2] Zhong, H.-S. *et al.* Quantum computational advantage using photons. *Science* **370**, 1460–1463 (2020).
- [3] Wang, H. *et al.* Toward Scalable Boson Sampling with Photon Loss. *Phys. Rev. Lett.* **120**, 230502 (2018).
- [4] Pelucchi, E. *et al.* The potential and global outlook of integrated photonics for quantum technologies. *Nat Rev Phys* **4**, 194–208 (2021).
- [5] Paesani, S. *et al.* Near-ideal spontaneous photon sources in silicon quantum photonics. *Nat Commun* **11**, 2505 (2020).
- [6] Silverstone, J. W., Bonneau, D., O’Brien, J. L. & Thompson, M. G. Silicon Quantum Photonics. *IEEE J. Sel. Top. Quantum Electron.* **22**, 390–402 (2016).
- [7] Wang, Y. *et al.* Deterministic photon source interfaced with a programmable silicon-nitride integrated circuit. *npj Quantum Inf* **9**, 94 (2023).
- [8] Senellart, P., Solomon, G. & White, A. High-performance semiconductor quantum-dot single-photon sources. *Nature Nanotech* **12**, 1026–1039 (2017).
- [9] Ding, X. *et al.* High-efficiency single-photon source above the loss-tolerant threshold for efficient linear optical quantum computing. *Nat. Photon.* **19**, 387–391 (2025).
- [10] Esmaeil Zadeh, I. *et al.* Superconducting nanowire single-photon detectors: A perspective on evolution, state-of-the-art, future developments, and applications. *Applied Physics Letters* **118**, 190502 (2021).
- [11] Schwartz, M. *et al.* Fully On-Chip Single-Photon Hanbury-Brown and Twiss Experiment on a Monolithic Semiconductor-Superconductor Platform. *Nano Lett.* **18**, 6892–6897 (2018). 1806.04099.
- [12] Reithmaier, G. *et al.* On-chip time resolved detection of quantum dot emission using integrated superconducting single photon detectors. *Sci Rep* **3**, 1901 (2013).

[13] Turunen, M. *et al.* Quantum photonics with layered 2D materials. *Nat Rev Phys* **4**, 219–236 (2022).

[14] Zotev, P. G. *et al.* Nanophotonics with multilayer van der Waals materials. *Nat. Photon.* **19**, 788–802 (2025).

[15] Montblanch, A. R., Barbone, M., Aharonovich, I., Atatiüre, M. & Ferrari, A. C. Layered materials as a platform for quantum technologies. *Nat. Nanotechnol.* **2023** *186* **18**, 555–571 (2023).

[16] Azimi, A. *et al.* Photonics in Flatland: Challenges and opportunities for nanophotonics with 2D semiconductors. *npj Nanophoton.* **2**, 44 (2025).

[17] Castellanos-Gomez, A. *et al.* Deterministic transfer of two-dimensional materials by all-dry viscoelastic stamping. *2D Mater.* **1**, 011002 (2014).

[18] Koperski, M. *et al.* Single photon emitters in exfoliated WSe₂ structures. *Nat. Nanotechnol.* **2015** *106* **10**, 503–506 (2015). 1411.2774.

[19] Parto, K., Azzam, S. I., Banerjee, K. & Moody, G. Defect and strain engineering of monolayer WSe₂ enables site-controlled single-photon emission up to 150 K. *Nat. Commun.* **12** (2021).

[20] Drawer, J.-C. *et al.* Monolayer-Based Single-Photon Source in a Liquid-Helium-Free Open Cavity Featuring 65% Brightness and Quantum Coherence. *Nano Lett.* **23**, 8683–8689 (2023).

[21] Paralikis, A. *et al.* Tailoring polarization in WSe₂ quantum emitters through deterministic strain engineering. *npj 2D Mater Appl* **8**, 1–8 (2024).

[22] Zhao, H., Pettes, M. T., Zheng, Y. & Htoon, H. Site-controlled telecom-wavelength single-photon emitters in atomically-thin MoTe₂. *Nat. Commun.* **2021** *121* **12**, 1–7 (2021).

[23] Wyborski, P. *et al.* Toward triggered generation of indistinguishable single-photons from MoTe₂ quantum emitters (2025). 2508.20743.

[24] Michaelis de Vasconcellos, S. *et al.* Single-Photon Emitters in Layered Van der Waals Materials. *Phys. Status Solidi B* **259**, 2100566 (2022).

[25] Wang, Y. *et al.* Enhancing Si3N4 Waveguide Nonlinearity with Heterogeneous Integration of Few-Layer WS₂. *ACS Photonics* **8**, 2713–2721 (2021).

[26] Ling, H., Li, R. & Davoyan, A. R. All van der Waals Integrated Nanophotonics with Bulk Transition Metal Dichalcogenides. *ACS Photonics* **8**, 721–730 (2021).

[27] Vyshnevyy, A. A. *et al.* Van der Waals Materials for Overcoming Fundamental Limitations in Photonic Integrated Circuitry. *Nano Lett.* **23**, 8064 (2023).

[28] Lee, S. W., Lee, J. S., Choi, W. H. & Gong, S. H. Ultrathin WS₂ Polariton Waveguide for Efficient Light Guiding. *Adv. Opt. Mater.* **11**, 2300069 (2023).

[29] Moore, S. L. *et al.* Van der Waals waveguide quantum electrodynamics probed by infrared nanophotoluminescence. *Nat. Photon.* (2025).

[30] Munkhbat, B., Küçüköz, B., Baranov, D. G., Antosiewicz, T. J. & Shegai, T. O. Nanostructured Transition Metal Dichalcogenide Multilayers for Advanced Nanophotonics. *Laser Photonics Rev.* **17** (2023). 2202.04898.

[31] Metuh, P. *et al.* Toward Single-Photon Detection with Superconducting Niobium Diselenide Nanowires. *ACS Photonics* **12**, 5912–5920 (2025).

[32] Zugliani, L. *et al.* 1 Single-photon detection in atomically thin NbSe₂ superconducting nanowires .

[33] Wang, H. *et al.* Emerging Single-Photon Detectors Based on Low-Dimensional Materials. *Small* **18**, 2103963 (2022).

[34] Errando-Herranz, C. *et al.* Resonance Fluorescence from Waveguide-Coupled, Strain-Localized, Two-Dimensional Quantum Emitters. *ACS Photonics* **8**, 1069–1076 (2021). 2002.07657.

[35] Blauth, M. *et al.* Coupling Single Photons from Discrete Quantum Emitters in WSe₂ to Lithographically Defined Plasmonic Slot Waveguides. *Nano Lett.* **18**, 6812–6819 (2018).

[36] Huang, X. *et al.* On-chip integrated light sources with MoS₂/WSe₂ moiré superlattices at telecom wavelengths (2025). 2504.03267.

[37] Kim, S. *et al.* Photonic crystal cavities from hexagonal boron nitride. *Nat Commun* **9**, 2623 (2018).

[38] Khelifa, R. *et al.* WSe₂ Light-Emitting Device Coupled to an h-BN Waveguide. *ACS Photonics* **10**, 1328–1333 (2023).

[39] Tonndorf, P. *et al.* On-Chip Waveguide Coupling of a Layered Semiconductor Single-Photon Source. *Nano Lett.* **17**, 5446–5451 (2017).

[40] Kim, S. *et al.* Integrated on Chip Platform with Quantum Emitters in Layered Materials. *Adv. Opt. Mater.* **7**, 1901132 (2019).

[41] Manzeli, S., Ovchinnikov, D., Pasquier, D., Yazyev, O. V. & Kis, A. 2D transition metal dichalcogenides. *Nat Rev Mater* **2**, 17033 (2017).

[42] Munkhbat, B., Wróbel, P., Antosiewicz, T. J. & Shegai, T. O. Optical Constants of Several Multilayer Transition Metal Dichalcogenides Measured by Spectroscopic Ellipsometry in the 300–1700 nm Range: High Index, Anisotropy, and Hyperbolicity. *ACS Photonics* **9**, 2398–2407 (2022).

[43] Barbone, M. *et al.* Charge-tunable biexciton complexes in monolayer WSe₂. *Nat Commun* **9**, 3721 (2018).

[44] Linhart, L. *et al.* Localized Intervalley Defect Excitons as Single-Photon Emitters in WSe₂. *Phys. Rev. Lett.* **123** (2019). 1904.03217.

[45] Desai, S. B. *et al.* Strain-Induced Indirect to Direct Bandgap Transition in Multilayer WSe₂. *Nano Lett.* **14**, 4592–4597 (2014).

[46] Kumar, S., Kaczmarczyk, A. & Gerardot, B. D. Strain-Induced Spatial and Spectral Isolation of Quantum Emitters in Mono- and Bilayer WSe₂. *Nano Lett.* **15**, 7567–7573 (2015).

[47] Piccinini, C. *et al.* High-purity and stable single-photon emission in bilayer WSe₂ via phonon-assisted excitation. *Commun Phys* **8**, 158 (2025).

[48] Munkhbat, B. *et al.* Transition metal dichalcogenide metamaterials with atomic precision. *Nat. Commun.* **11** (2020). 2002.05696.

[49] Ling, H. *et al.* Deeply subwavelength integrated excitonic van der Waals nanophotonics. *Opt. Vol 10 Issue 10 Pp 1345-1352* **10**, 1345–1352 (2023).

[50] Peyskens, F., Chakraborty, C., Muneeb, M., Van Thourhout, D. & Englund, D. Integration of single photon emitters in 2D layered materials with a silicon nitride photonic chip. *Nat Commun* **10**, 4435 (2019).

[51] Casses, L. N., Kaltenegger, K. J., Xiao, S., Wubs, M. & Stenger, N. Quantitative near-field characterization of surface plasmon polaritons on monocrystalline gold platelets. *Opt. Express*, *OE* **30**, 11181–11191 (2022).

[52] Casses, L. N. *et al.* Full Quantitative Near-Field Characterization of Strongly Coupled Exciton–Plasmon Polaritons in Thin-Layered WSe₂ on a Monocrystalline Gold Platelet. *ACS Photonics* **11**, 3593–3601 (2024).

[53] Cheng, L., Mao, S., Li, Z., Han, Y. & Fu, H. Y. Grating couplers on silicon photonics: Design principles, emerging trends and practical issues. *Micromachines* **11** (2020).

[54] Zhu, Y. *et al.* Ultra-compact silicon nitride grating coupler for microscopy systems. *Opt. Express* **25**, 33297 (2017).

[55] Chen, X., Li, C. & Tsang, H. K. Fabrication-Tolerant Waveguide Chirped Grating Coupler for Coupling to a Perfectly Vertical Optical Fiber. *IEEE Photonics Technol. Lett.* **20**, 1914–1916 (2008).

[56] Mitryakhin, V. N. *et al.* Rabi oscillations of a monolayer quantum emitter driven through its excited state (2025). 2510.23222.

[57] Paralikis, A., Wyborski, P., Metuh, P., Gregersen, N. & Munkhbat, B. Tunable and Low-Noise WSe₂ Quantum Emitters for Quantum Photonics. *PRX Quantum* **6**, 040339 (2025).

[58] Rodiek, B. *et al.* Experimental realization of an absolute single-photon source based on a single nitrogen vacancy center in a nanodiamond. *Optica* **4**, 71–76 (2017).

[59] Iff, O. *et al.* Purcell-Enhanced Single Photon Source Based on a Deterministically Placed WSe₂ Monolayer Quantum Dot in a Circular Bragg Grating Cavity. *Nano Lett.* **21**, 4715–4720 (2021).

[60] Binkowski, F. *et al.* High Purcell enhancement in all-TMD nanobeam resonator designs with active monolayers for nanolasers. *Phys. Rev. B* **112**, 235410 (2025).

[61] Vannucci, L. *et al.* Single-photon emitters in WSe₂ : Critical role of phonons on excitation schemes and indistinguishability. *Phys. Rev. B* **109**, 245304 (2024).

[62] Raschke, M. B. & Lienau, C. Apertureless near-field optical microscopy: Tip–sample coupling in elastic light scattering. *Appl. Phys. Lett.* **83**, 5089–5091 (2003).

[63] Knoll, B. & Keilmann, F. Enhanced dielectric contrast in scattering-type scanning near-field optical microscopy. *Optics Communications* **182**, 321–328 (2000).

[64] Ocelic, N., Huber, A. & Hillenbrand, R. Pseudo-heterodyne detection for background-free near-field spectroscopy. *Appl. Phys. Lett.* **89**, 101124 (2006).